



Hierarchically designed ZIF-8-derived Ni@ZnO/carbon nanofiber freestanding composite for stable Li storage

Bhavana Joshi^{a,1}, Edmund Samuel^{a,1}, Yong Il Kim^a, Min-Woo Kim^a, Hong Seok Jo^a, Mark T. Swihart^b, Woo Young Yoon^{c,*}, Sam S. Yoon^{a,*}

^a School of Mechanical Engineering, Korea University, Seoul 136-713, Republic of Korea

^b Department of Chemical & Biological Engineering, University at Buffalo, The State University of New York, Buffalo, NY 14260-4200, USA

^c Department of Materials Science & Engineering, Korea University, Seoul 02841, Republic of Korea

HIGHLIGHTS

- Carbon wrapped with bimetallic Ni@ZnO was decorated on carbon nanofibers via chemical surface treatment.
- The composite electrode showed highly stable electrochemical performance during long-term cycling.
- The superior performance is attributed to synergy of Ni@ZnO (high capacity) and carbon (stability).

ARTICLE INFO

Keywords:

Ni@ZIF-8
MOF
Nanofiber
Lithium ion battery
Anode

ABSTRACT

We present a uniform rhombohedral Ni@ZnO bimetallic oxide host over carbon nanofibers (CNF) as an anode material for Li-ion batteries. Ni@ZnO was produced by annealing a Ni@zeolitic imidazolate framework (ZIF-8) hierarchically decorated over CNFs. The rationally-designed freestanding composite exhibited promising stability in electrochemical performance. A first reversible capacity of 1051 mA·h·g⁻¹ was measured at a current density of 100 mA·g⁻¹, and 88% of this capacity was retained after 100 cycles. We attribute this high capacity retention to the hierarchical structure of the Ni@ZnO-enwrapped carbon framework encapsulating the conductive CNFs, as demonstrated by scanning and transmission electron microscopy. The composite electrode also showed a high specific capacity of ~497 mA·h·g⁻¹ in high-rate testing at 1000 mA·g⁻¹, because the cage-like framework of the material allowed rapid charge transfer and Li-ion diffusion in the anode.

1. Introduction

The need for sustainable energy storage devices has increased significantly with improvements in electric bicycles, hybrid electric vehicles, and flexible electronics. [1–3] Improving the performance of these energy storage devices requires advances in Li storage for the further development of Li ion batteries (LIBs). Commercially, graphite is used as the anode material in LIBs, but it has a relatively low theoretical capacity of 372 mA·h·g⁻¹. [4] Thus, a primary focus in LIB research is the improvement of the specific capacity of LIB anode materials to overcome their limitations for Li storage. [5–7] The synthesis of new materials is essential to achieving high and long-term capacity, energy density, and stability.

Alloys [8] and transition metal oxides (TMOs) [9–11] can have very high capacities because they combine intercalation, conversion, and Li

alloy formation mechanisms that could provide enhanced energy density. [12,13] However, alloys and TMOs suffer from high volume expansion and contraction upon lithiation and delithiation. The volume changes of alloys and TMOs during lithiation/de-lithiation limit their electrochemical performances and can induce rapid capacity fading. To address this issue, many researchers have investigated composites of metal oxides and carbon allotropes. [9,14,15] Carbon allotropes, including carbon black, carbon nanotubes, and graphene, possess intercalation/deintercalation mechanisms to host Li ions and stabilize metal oxides in composites. [16] In general, carbon is used either to improve the anode conductivity or to provide shells for metal oxides and alloys to alleviate agglomeration. [17,18] The carbon shell improves the anode stability by mitigating pulverization effects and buffering volume expansion/contraction strains.

Recently, metal–organic frameworks (MOF) comprising porous,

* Corresponding authors.

E-mail addresses: wyyoon@korea.ac.kr (W.Y. Yoon), skyoony@korea.ac.kr (S.S. Yoon).

¹ These authors have contributed equally.

cage-like crystalline structures of self-assembled metal ions and organic ligands have received significant attention for LIB applications. [19,20] Air-calcined MOF-derived TMOs show peculiar shapes and nanoporous structures. [21] The controlled pore structures and redox activities of various MOFs such as MIL (Materials of Institute Lavoisier) 53 [22], MIL 68 [23], Fe MOF [24], MIL 88 [25], zeolitic imidazole framework (ZIF) 67 [26], Ni MOF [27], and Ni MIL 77 [28] have been reported for use in LIB anodes. Transition metal sulfide [29–31] and TMO/carbon composites derived from MOFs are an important area of investigation. Such composites could produce well-dispersed nanoparticles in a porous carbon matrix wherein the carbon shell could protect the active material from pulverization or aggregation. [32,33]

Here, we report a Ni-assembled ZIF-8 as a bimetallic MOF loaded on carbon nanofibers (CNF). The annealing of this MOF in Ar yielded a Ni@ZnO/CNF composite. In the composite, Ni and Zn/ZnO are present at edge sites of carbon/N cages derived from methyl imidazole. The carbon cage and N heteroatoms promote the specific capacity and stability of the material by forming a conductive network as well as a ZnO volume-buffering framework. The carbonized framework retains a truncated rhombohedral shape along with native porosity, which provides a paths for rapid Li-ion insertion and extraction. Ni contributes to the capacity through conversion reactions with Li₂O and Zn, forming Li–Zn alloys. We present here a facile, scalable, and low-cost process for the fabrication of hierarchically designed freestanding ZIF-8-derived composites showing superior electrochemical performance for Li storage, and compare their performance to that of the other MOF-derived materials discussed above.

2. Experimental procedure

2.1. Precursor and electrospinning

The Ni@ZIF-8-loaded fiber preparation includes three steps: (1) electrospinning, (2) Ni@ZIF-8 precipitation, and (3) loading Ni@ZIF-8 on CNFs. In the first step, we prepared a solution of 8 wt% polyacrylonitrile (PAN, $M_w = 150$ kDa, Sigma-Aldrich) and 0.8 wt% 2-methyl imidazole (2MI, Sigma-Aldrich) in N,N-dimethylformamide (DMF, 99.8%, Sigma-Aldrich) by mixing and stirring for 24 h. Then, fibers of PAN/2MI were electrospun for 2 h at a solution flowrate of 250 $\mu\text{L}/\text{h}$ at a constant voltage of 7 kV, which produced a stable Taylor cone; the fibers were collected on a drum collector rotating at 200 rotations per minute (rpm).

In the second step, we prepared 50 mL of a Ni@ZIF-8 precursor solution containing zinc acetate dihydrate (10 mM) and varying concentrations of nickel nitrate hexahydrate (3, 5, or 7 mM) in methanol. After dissolution of metal salts, 40 mM of 2MI was added and the solution was stirred for 10 min, during which time it transformed from a transparent light green-colored solution to a cloudy green dispersion of particles. The addition of the Ni salt induced the green color; as the Ni concentration was increased, the green color became darker. In addition, a mixture of only nickel nitrate hexahydrate and 2MI in methanol (without zinc acetate dihydrate) yielded no precipitate.

For the third step, the PAN/2MI fibers were soaked in a Ni@ZIF-8 solution for 1 h 50 min, yielding Ni@ZIF-8-decorated fibers. These fibers were washed with clean methanol and further allowed to dry for 24 h at room temperature of 20 °C. Particle loading did not occur on PAN fibers that did not contain 2MI. This suggested that the 2MI/PAN surface worked as a template for ZIF-8 growth; the imidazolium ions from the 2MI ligands reacted with Zn²⁺ from the zinc acetate/methanol solution. Zn²⁺ was linked to imidazolium ions via N atoms, forming rhombohedral shapes in which the metal–ligand–metal bonds are oriented at an angle of 145°. As mentioned earlier, Ni did not react with 2MI; thus, we believe the Ni ions became connected with Zn in the ZIF-8 structures. Schematics depicting Ni@ZIF-8 loading on 2MI/PAN fibers are presented in Fig. 1.

The dried fibers were stabilized at 150 °C for 30 min at a ramp rate

of 5 °C/min, followed by heating under Ar a ramp rate of 3 °C/min to 700 °C and carbonizing the fibers for 1 h at that temperature. The obtained fibers were freestanding and black in color. Based on the Ni concentration in the precursor solution, the carbonized Ni@ZIF-8-derived fibers were labeled as 3Ni, 5Ni, and 7Ni.

2.2. Characterization

The microstructural characteristics of the composite fibers were analyzed by field-emission scanning electron microscopy (FESEM; S-5000, Hitachi, Ltd.) at an acceleration voltage of 15 kV and by transmission electron microscopy (TEM; JEM 2100F, JEOL Inc.). The crystallographic structure of the sample was evaluated by X-ray diffraction (XRD, SmartLab, Rigaku diffractometer) using Cu K α radiation over a 2 θ range of 5°–80°. The graphitic transformation of the PAN nanofiber/organic ligand to CNF was studied by Raman spectroscopy (Jasco, NRS-3100) using a 532-nm exciton laser. The chemical states of the composite fibers were investigated by X-ray photoelectron spectroscopy (XPS; Theta Probe Base System, Thermo Fisher Scientific Co.) with Al K α radiation at an energy of 25 W in a vacuum of 10^{−7} Pa. The surface areas of composites were measured by nitrogen physisorption in a volumetric adsorption apparatus (Tristar 3000, Micromeritics). The sample was pretreated at 300 °C for 48 h under high vacuum (< 10^{−6} Torr) before measuring adsorption/desorption isotherms.

Electrochemical measurements were performed using CR2032 Li half-cells. The freestanding active composite mat with a density of 0.9 mg·cm^{−2} was used as the working electrode; the counter electrode was Li foil. The electrodes were separated by a Celgard 2400 polymer separator (Celgard, Chungbuk, South Korea). All tests were conducted in an electrolyte solution containing 1 M LiPF₆ dissolved in ethylene carbonate, dimethyl carbonate, and ethyl methyl carbonate (1:1:1 by volume) (PuriEL, Soulbrain, Seongnam, South Korea). The galvanostatic charge/discharge curves were recorded using a WBCS3000 battery cycler (WonATech, Seoul, South Korea). Electrochemical impedance spectroscopy (EIS) was conducted using a potentiostat (VersaSTAT-3, Princeton Applied Research, USA) with a perturbation potential of 10 mV over a frequency range of 100 kHz to 0.01 Hz. All measurements were conducted at room temperature.

3. Results and discussion

The XRD patterns for the Ni@ZnO/CNF composites annealed at 700 °C in Ar are as shown in Fig. 2a. The peak at 28° and the double peak at 47° and 56° are well matched with JCPDS No. 21-1486 and 36-1451, respectively, indicating the formation of ZnO in Ni@ZnO over the composite CNF. However, with increasing Ni content, ZnO formation is apparently restricted, possibly because the increase of metallic atoms and the annealing in Ar restricts the further crystallization of ZnO/NiO with limited O₂ available. No NiO peaks are revealed in the XRD pattern. The carbon from CNF, as well as that covered by ZnO/NiO in the ZIF-8 framework, is amorphous in form, as evidenced by the broad peak at 22°. For confirmation of ZIF8 and NiZIF8 loading over fiber the XRD of as-synthesized (before carbonization) samples are presented in Supporting Information Fig. S1. The XRD compared with simulated data presented in a patent [34] shows consistent diffraction peaks that confirms loading of ZIF8. Addition of Ni resulted in negligible alteration of the ZIF8 structure.

The impact of Ni concentration on the carbon structural disorder was surveyed by Raman spectroscopy, as presented in Fig. 2b. The D and G bands associated with disordered (*sp*³) and crystalline graphitic (*sp*²) carbon are observed at approximately 1350 and 1580 cm^{−1}, respectively. The *I*_D/*I*_G ratio, reflecting the degree of carbon crystallinity, decreases notably from 1.28 to 1.02 as the Ni concentration is increased from 3 to 7 mM. The presence of Ni is known to catalyze graphene growth at high temperatures; thus, this result is not surprising. [35] Lower defect levels in graphitic carbon increase the conductivity, but

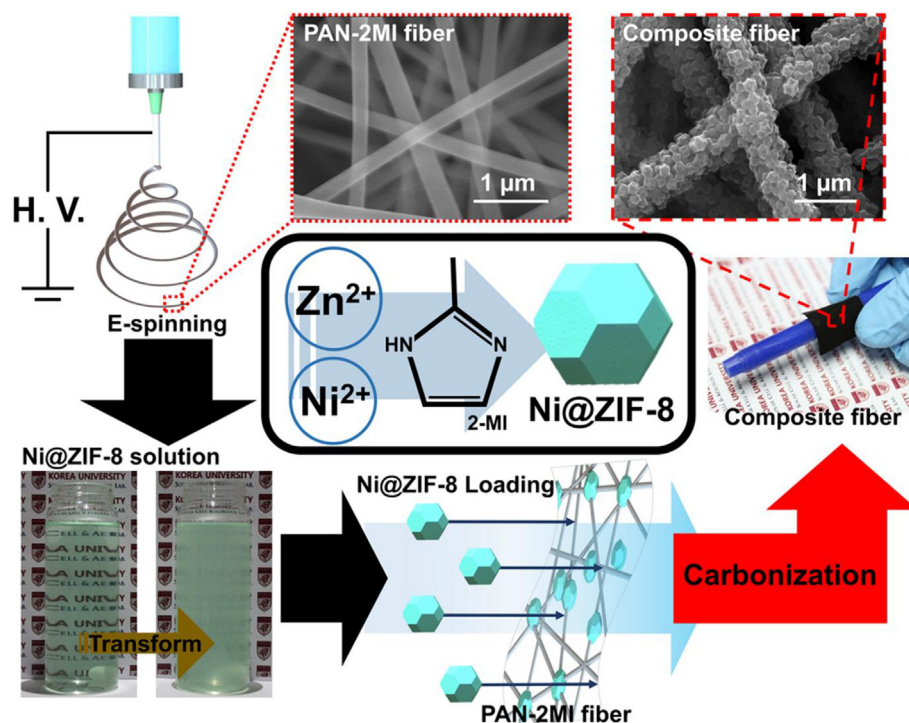


Fig. 1. Schematic of the fabrication of Ni@ZIF-8 fibers and carbonization thereof, yielding flexible, freestanding Ni@ZnO composite fibers.

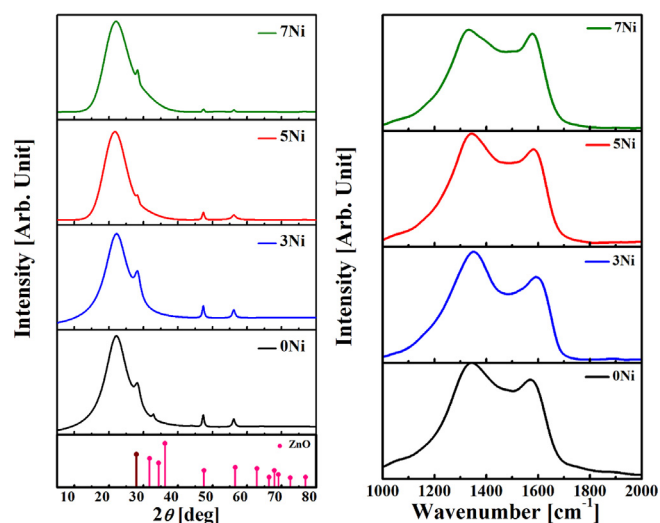


Fig. 2. (a) XRD patterns and (b) Raman spectra of carbonized Ni@ZnO composites.

simultaneously limit Li storage. [9,11] The blue shift appearing in the D and G bands, along with the increase in graphitic content, may relate to compressive strain generated by the presence of Ni. [36]

FESEM images of the carbonized Ni@ZIF-8, i.e., Ni@ZnO (3Ni), are shown in Fig. 3a and b. The addition of Ni promotes uniform crystal growth covering the fiber with polyhedral particles. Thus, the well-grown particles induced by Ni doping provide more area for Li storage. On the other hand, when Ni (0Ni) was removed, random shapes or distorted polyhedral of carbonized ZIF-8 particles were formed on CNF, as shown in Fig. 3c and d. In addition, following carbonization, dimples are formed on these polyhedral-shape particles, which may reduce lithium hosting sites. The elemental mapping shown in Fig. 4 demonstrates that the Ni, Zn, C, O, and N are homogeneously distributed, suggesting the absence of phase segregation. Details of the elemental concentrations of 0, 3, 5 and 7Ni@ZnO are presented in Supporting

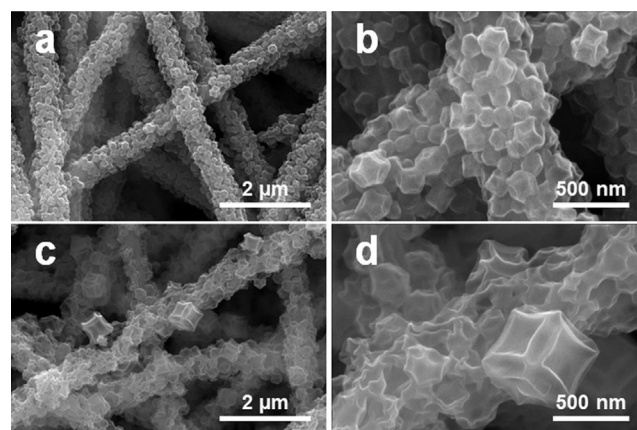


Fig. 3. SEM images of (a, b) carbonized Ni@ZnO/CNF composite (3Ni) and (c, d) carbonized ZnO/CNF (0Ni).

Information Table S1.

The chemical states of the elements in the composite fiber mat were evaluated by XPS. Fig. 5a shows the survey spectrum indicating the presence of Zn, O, Ni, C, and N, consistent with the energy-dispersive X-ray spectroscopy (EDX) mapping in Fig. 4 and values in Table S1. The high-resolution core spectrum of the Zn 2p orbital (Fig. 5b) shows two obvious peaks at 1022 and 1044 eV for Zn 2p_{3/2} and Zn 2p_{1/2}, respectively. The 22.5 eV binding energy difference between the spin-orbit splitting of Zn 2p demonstrates the existence of Zn²⁺. The O 1s spectrum presented in Fig. 5c shows a peak at 532 eV assigned to O²⁻ ions in ZnO, as confirmed by the deconvoluted lattice O peak at 530.1 eV. The other three deconvoluted peaks belong to non-lattice O (oxygen near an oxygen vacancy or a point defect, Vo), Zn–O–H, and O–H coming from moisture adsorption. [37] The Ni 2p core spectrum depicted in Fig. 5d shows two characteristic peaks at 856 and 871 eV, attributed to 2p_{3/2} and 2p_{1/2} respectively. The spin-orbit splitting produces an energy difference of 15.5 eV, possibly because of proximity to O-containing functional groups. Further, the deconvolution of the

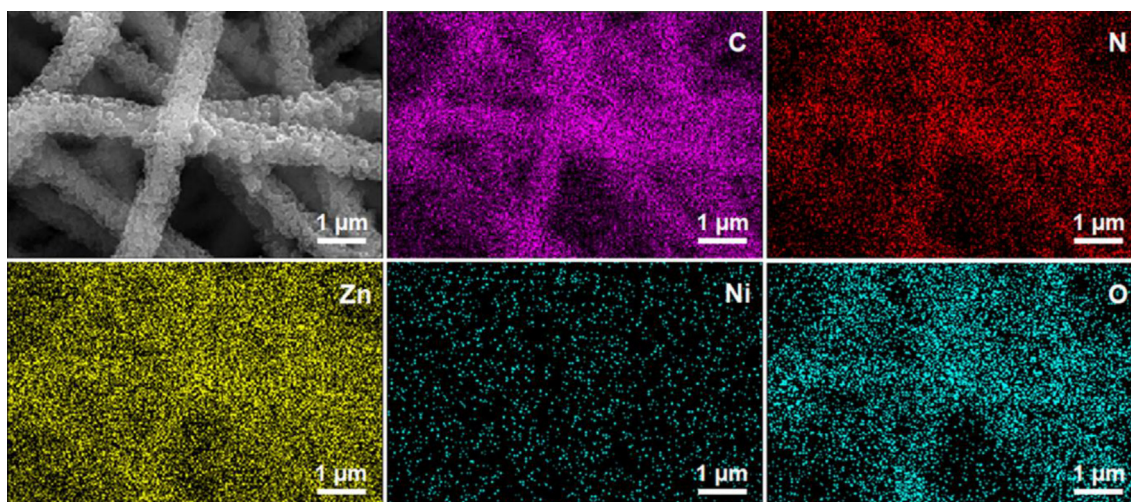


Fig. 4. Elemental mapping of carbonized Ni@ZnO/CNF composite (3Ni).

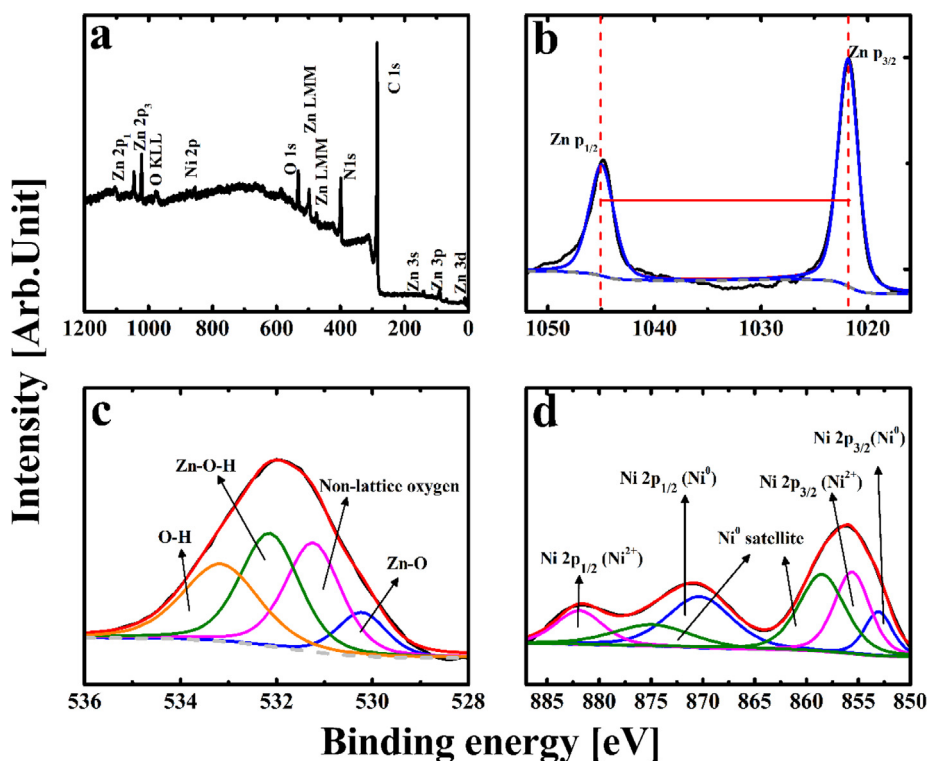


Fig. 5. (a) Survey XPS spectrum; core spectra of (b) Zn, (c) O, and (d) Ni.

spectrum reveals peaks at 853.0 and 870.3 eV from Ni^0 and at 855.6 and 881.89 eV from Ni^{2+} . The satellite peaks at 858.4 and 874.8 eV are also attributed to Ni^0 . [38,39]

The structural features of the composite fiber were also scrutinized by TEM, high-resolution TEM (HRTEM), and selected-area electron diffraction (SAED). The TEM image of the composite fiber in Fig. 6a is a magnified version of Fig. 6b that clearly shows the loading of cage-type structures, retained by the carbon framework produced from 2MI, over the CNF. Hollow areas formed by the porous nature of ZIF-8 and dark edges are clearly observed in the TEM images. This hollow area suggests the presence of porosity, which was confirmed by Brunauer-Emmett-Teller (BET) analysis (see Fig. S2) where measured surface areas were 31.6 and 38.6 m^2/g for 0 and 3Ni@ZnO. No clear lattice spacing is observed in low- or high-resolution HRTEM (Fig. 6c and 6d, respectively), but the SAED pattern demonstrates a ring corresponding to the

(102) plane of ZnO, consistent with the peak at 47° in the XRD pattern. Furthermore, the elemental mapping in Fig. 6e shows Ni, Zn and O along with C are consistently distributed within the ZIF-8-derived particles.

The electrochemical performance of the annealed Ni@ZnO/CNF structures with different Ni concentrations (0Ni, 3Ni, 5Ni, and 7Ni) was tested in LIB half-cells. The presence of the Ni@ZnO on the CNFs provides stable rate capability under various current densities from 100 to 1000 $\text{mA}\cdot\text{g}^{-1}$ for 100 cycles (N). The ZIF-8-derived carbon framework decreases the transport/diffusion path length for both electrons and Li ions, yielding better rate capability. Furthermore, the presence of Ni and Zn in the bimetallic organic framework (BmOF) buffers the strain during the volume expansion and contraction of ZnO during lithiation and de-lithiation, respectively, while the CNF enforces the mutual connection between the active materials and electrolyte by offering

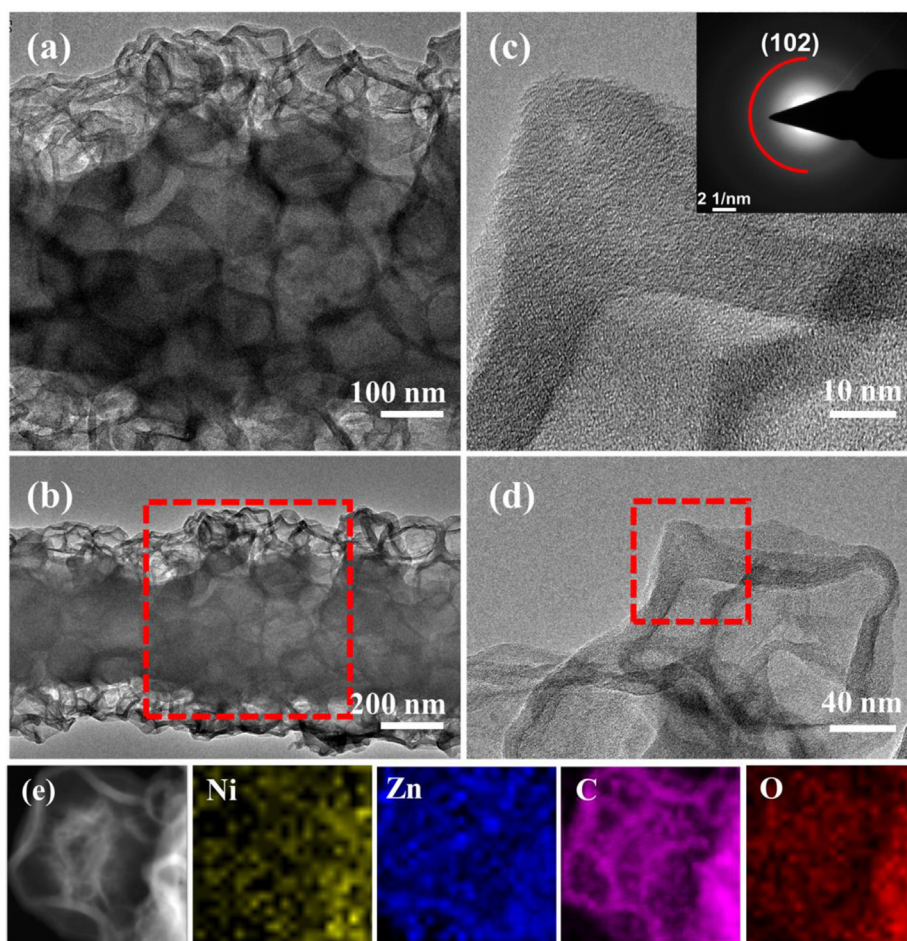


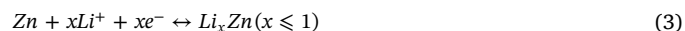
Fig. 6. (a), (b) TEM images, (c), (d) HRTEM images. Inset of (c): SAED pattern. (e) Elemental mapping of carbonized Ni@ZnO/CNF composite (3Ni).

conductive pathways. The BmOF interconnected structure supplies additional accessible redox sites for Li ion storage. [17] The first discharge specific capacities of 3Ni, 5Ni, and 7Ni are 1484, 1293, and 1208 mA·h·g⁻¹ respectively. The sample 3Ni exhibits superior electrochemical performance compared to the 5Ni and 7Ni samples. The average values of specific capacity during rate capability testing shown in Fig. 7a at different current densities of 100 (*N* = 50), 200 (*N* = 20), 500 (*N* = 20), and 1000 (*N* = 10) mA·g⁻¹ are 940, 823, 639, and 497 mA·h·g⁻¹, respectively.

The long-term cycling performances of 0Ni, 3Ni, 5Ni, and 7Ni at 100 mA·g⁻¹ for 100 cycles are shown in Fig. 7b. The 0Ni sample, included for reference, contains only ZIF-8-derived ZnO/CNF. The first discharge/charge capacities of these samples were 1234/854, 1547/1100, 1359/937, and 1200/840 mA·h·g⁻¹, respectively. The high Coulombic efficiency (CE) exhibited at *N* = 1 by all samples exceeds 69%, suggesting the formation of a thin solid electrolyte interface (SEI) layer benefiting from the retained zeolitic organic framework. In the subsequent cycling performance, CE exceeds 98% for all samples and thereafter remains constant. The corresponding reversible capacities at *N* = 2 for 0Ni, 3Ni, 5Ni, and 7Ni are 742, 1051, 898, and 810 mA·h·g⁻¹. The highest reversible capacity retention after 100 cycles is ~88% for 3Ni. In comparison with previously reported MOF and MOF-derived LIB anodes, listed in Table 1, the freestanding composite synthesized here shows highly stable performance.

Fig. 7c presents the charge/discharge curves of 3Ni at the current density of 100 mA·g⁻¹. The initial discharge capacity of the 3Ni composite is 1547 mA·h·g⁻¹, followed by the reversible capacity of 1051 mA·h·g⁻¹. The galvanostatic charge/discharge profile presented in Fig. 7c shows that the anode possesses a high specific capacity and

good reversibility. The excellent CE of 71% for the first cycle indicates reversible delithiation. CE quickly reaches 98% during the second cycle and remains constant at ~99%. The CE exhibited during galvanostatic cycling from *N* = 5 onward suggests complete deintercalation of Li ions with no further SEI formation or any other irreversible losses, owing to the hierarchical structure of the Ni@ZnO/CNF composites. The high reversible capacity of the anode material involves three major reversible reactions during lithiation/de-lithiation. In the course of anodic lithiation, the electrochemical reactions are: (1) the reduction of ZnO to metallic Zn by lithiation, yielding Li₂O; (2) the reaction of NiO with lithium that forms Ni and Li₂O along with reversible reaction of Ni to form NiO; and (3) alloying of free Zn, as shown as follows.



All these reactions are clearly reversible, as observed consistently from current rate measurement, long-term cycling, and charge/discharge profiles. Thus, during de-lithiation, ZnO, Ni, and Zn are recovered. Herein, the role of Ni becomes significant in the conversion of Li₂O to Li by the reversible reaction shown as equation 2; thus, Ni supports the enhanced capacity retention.

To evaluate the electrochemical performance of 3Ni, we studied the differential capacity. Fig. 7d shows the differential capacity variation relative to voltage for the first two discharge cycles of the 3Ni sample. Two clear distinct peaks are observed at 0.74 and 0.55 V. The sharp peak at 0.74 V corresponds to SEI layer formation. However, this peak vanishes from the second cycle onward, suggesting that SEI layer

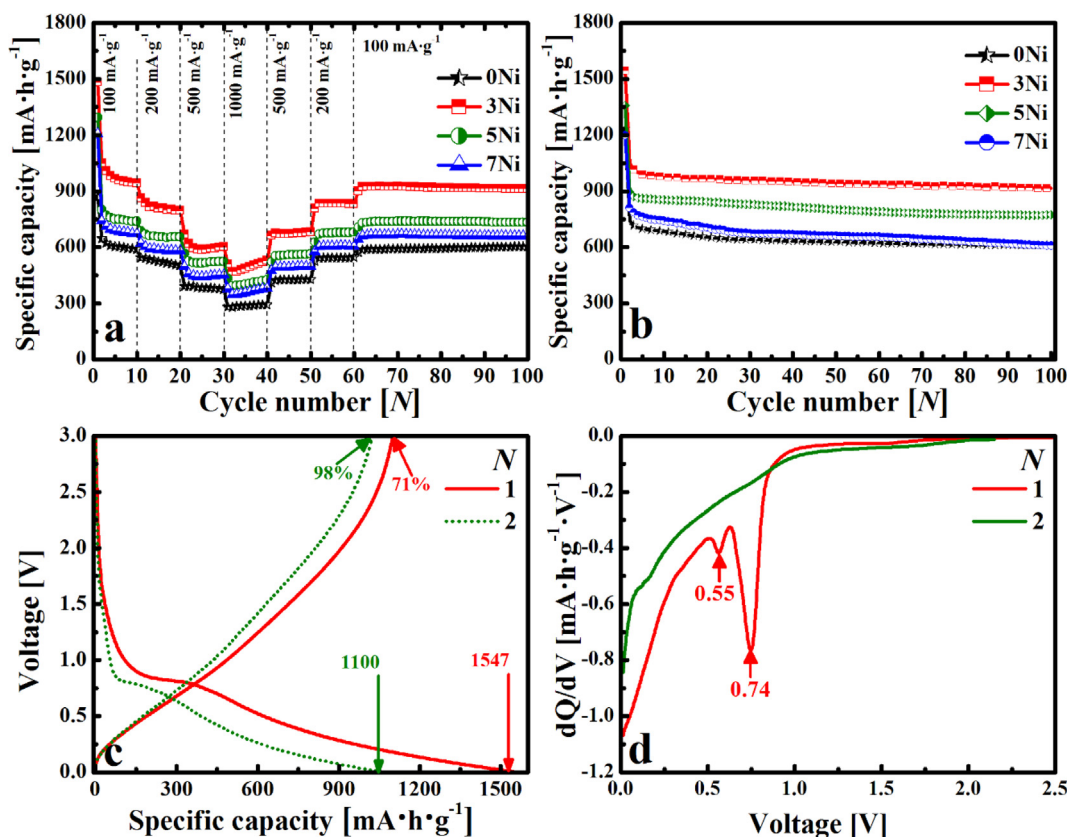


Fig. 7. (a) Rate-dependent capacity measurements over a voltage range of 0.01–3 V, (b) long-term cycling performance at a current density of 100 mA·g⁻¹, (c) galvanostatic charge/discharge profiles for initial cycles, and (d) differential capacity curves during lithiation.

formation is completed during the first discharge cycle. The second peak at 0.55 V corresponds to the reduction of ZnO to metallic Zn and later to its alloying with Li ions as Li–Zn [40]. The low intensity broad peak at ~1.47 V (see Fig. S3b inset) may correspond to the reduction of NiO according to the reaction given by Eq. (2). [41] In the differential capacity delithiation curve during the cycling, first broad oxidation peak corresponds to the de-alloying process of the products of Li_xZn_y as shown in Fig. S3b. The oxidation peaks in the dQ/dV curve (Fig. 3a) at around ~1.2 and 2.2 V relate to decomposition of Li₂O and the formation ZnO and NiO from metallic Zn and Ni respectively in accordance with the reactions of eqn (1) and (2). [41,42]

The peak in the subsequent cycle is shifted to 0.27 V and is significantly reduced in intensity. The decreased ZnO peak intensity during the second cycle may originate from the formation of NiO and ZnO together, which can cause structural modifications of ZnO at the hosting sites of the sustained bimetallic zeolitic framework (see TEM images in Fig. 6). However, the SEM images of fibers after cycling, presented in Supporting Information Fig. S4, show intact fibers covered with an SEI layer.

Table 1
Comparison of various MOF-based electrodes with Ni@ZnO/CNF derived from ZIF-8.

MOF	Freestanding	Discharge capacity [mA·h·g ⁻¹]	Charge capacity [mA·h·g ⁻¹]	Reversible capacity [mA·h·g ⁻¹] @Nth cycle	Rate [mA·g ⁻¹]	Ref.
MIL 53	No	93	77.5	73@8	C/10	[22]
MIL 68	No	40	31	32@12	C/50	[23]
Ni MIL77	No	743	519	700@60	100	[28]
Ni MOF	No	1984	1369	620@100	100	[27]
ZIF 67	No	1317	921	780@100	100	[26]
MIL 88	No	–	–	864@50	200	[25]
Fe MOF	No	1487	1024	1024@40	100	[24]
Zn/Ni MOF	No	1221	769	1008.6@200	100	[43]
Ni@ZnO (Ni@ZIF-8)	Yes	1547	1100	1051@100	100	Present

Fig. 8 shows typical Nyquist plots for 3Ni, 5Ni, and 7Ni samples of the Ni@ZnO/CNF composite under open-circuit conditions. The Nyquist plots were fitted to an appropriate Randle equivalent circuit, as shown in the inset of Fig. 8a, using Zsimp software. To visualize the semicircular arc in the high-frequency region, a magnified view of the Nyquist plot is presented in Fig. 8b. The straight line at intermediate to low frequencies suggests excellent diffusion and fast kinetic reactions for all tested anode materials. The Lithium ion diffusion coefficient estimated from the Warburg region, shown in Supporting Information Fig. S5, indicates faster Li ion diffusion in 3Ni samples. The rapid diffusion in the 3Ni samples is consistent with their high retention capacity shown during long-term cycling, as shown in Fig. 7b. The high-frequency x-intercept is the solution resistance (R_s), while the high- to intermediate-frequency intercept at the second edge of the semicircular arc corresponds to the charge transfer resistance (R_{ct}). The R_s values of 0.2, 0.75, and 1.3 Ω and R_{ct} values of 131, 112, and 72 Ω were obtained from the spectra for 3Ni, 5Ni, and 7Ni, respectively. All samples show low R_s and R_{ct} values, suggesting good conductivity of the BmOF hosted on CNF.

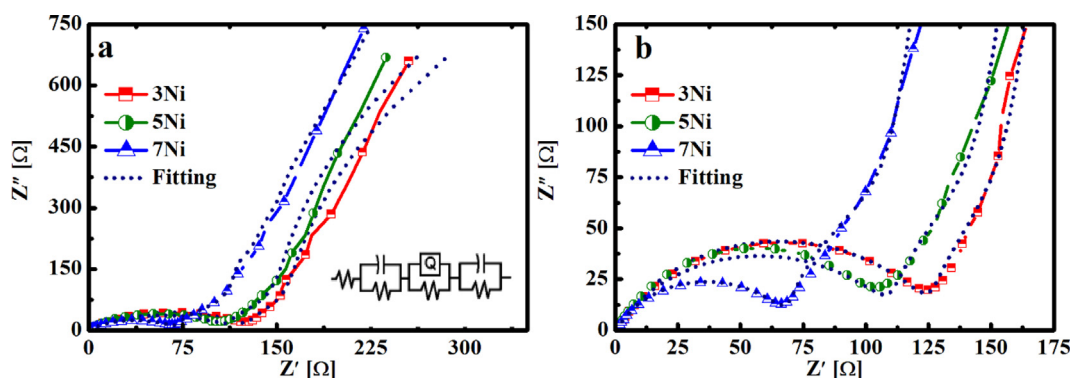


Fig. 8. Electrochemical impedance spectroscopy. (a) Nyquist plot. Inset: equivalent circuit. (b) Magnified Nyquist data.

4. Conclusions

Hierarchical Ni@ZIF-8 over PAN/2MI nanofibers were carbonized to a porous carbon wrapped with Ni@ZnO. In the presence of catalytic Ni, no concave strain was observed in the crystallites; perfect rhombohedral Ni@ZnO was retained, as verified by SEM and TEM. The optimum electrode (3Ni) showed stable cycling performance with 88% specific capacity retention from the 2nd to the 100th cycle, because of its unique morphology and buffering reactions by Ni. This simple and cost-effective carbonized Ni-containing ZIF-8 decorated on CNF after annealing in Ar provided freestanding anode materials showing improved conductivity and high capacity. The facile approach demonstrated here is promising for the scalable fabrication of anodes with high lithium storage capacities.

Acknowledgements

This research was supported by the Technology Development Program to Solve Climate Changes of the National Research Foundation (NRF) funded by the Ministry of Science, ICT & Future Planning (NRF-2016M1A2A2936760) and NRF-2017R1A2B4005639.

Appendix A. Supplementary data

Supplementary data associated with this article can be found, in the online version, at <http://dx.doi.org/10.1016/j.cej.2018.05.098>.

References

- Y. Zhao, X. Li, J. Liu, C. Wang, Y. Zhao, G. Yue, MOF-derived ZnO/Ni₃ZnCo_{0.7}/C hybrids yolk-shell microspheres with excellent electrochemical performances for lithium ion batteries, *ACS Appl. Mater. Interfaces* 8 (2016) 6472–6480.
- L. Wang, Y. Han, X. Feng, J. Zhou, P. Qi, B. Wang, Metal-organic frameworks for energy storage: batteries and supercapacitors, *Coord. Chem. Rev.* 307 (2016) 361–381.
- X. Wang, L. Wang, B. Chen, J. Yao, H. Zeng, MOFs as reactant: In situ synthesis of Li₂ZnTi₃O₈@C-N nanocomposites as high performance anodes for lithium-ion batteries, *J. Electroanal. Chem.* 775 (2016) 311–319.
- P.Q. Yuzhen Han, Siwu Li, Xiao Feng, Junwen Zhou, Haiwei Li, Su Shuangyue, Xingguo Li, Bo Wang, A novel anode material derived from organic-coated ZIF-8 nanocomposites with high performance in lithium ion batteries, *Chem. Commun.* 50 (2014) 8057–8060.
- Z. Chen, R. Wu, H. Wang, Y. Jiang, L. Jin, Y. Guo, Y. Song, F. Fang, D. Sun, Construction of hybrid hollow architectures by in-situ rooting ultrafine ZnS nanorods within porous carbon polyhedra for enhanced lithium storage properties, *Chem. Eng. J.* 326 (2017) 680–690.
- Y. Liao, C. Li, X. Lou, P. Wang, Q. Yang, M. Shen, B. Hu, Highly reversible lithium storage in cobalt 2,5-dioxido-1,4-benzenedicarboxylate metal-organic frameworks boosted by pseudocapacitance, *J. Colloid. Interface Sci.* 506 (2017) 365–372.
- X. Chen, Y. Huang, K. Zhang, Cobalt nanofibers coated with layered nickel silicate coaxial core-shell composites as excellent anode materials for lithium ion batteries, *J. Colloid Interface Sci.* 513 (2017) 788–796.
- M.N. Obrovac, V.L. Chevrier, Alloy negative electrodes for Li-ion batteries, *Chem. Rev.* 114 (2014) 11444–11502.
- E. Samuel, H.S. Jo, B. Joshi, S. An, H.G. Park, Y. Il Kim, W.Y. Yoon, S.S. Yoon, Decoration of MnO nanocrystals on flexible freestanding carbon nanofibers for lithium ion battery anodes, *Electrochim. Acta* 231 (2017) 582–589.
- W. Zhuang, L. Lu, W. Li, R. An, X. Feng, X. Wu, Y. Zhu, X. Lu, In-situ synthesized mesoporous TiO₂-B/anatase microparticles: Improved anodes for lithium ion batteries, *Chin. J. Chem. Eng.* 23 (2015) 583–589.
- B. Joshi, E. Samuel, M.-W. Kim, S. Park, M.T. Swihart, W.Y. Yoon, S.S. Yoon, Atomic-layer-deposited TiO₂-SnZnO/carbon nanofiber composite as a highly stable, flexible and freestanding anode material for lithium-ion batteries, *Chem. Eng. J.* 338 (2018) 72–81.
- Z. Wang, D. Luan, S. Madhavi, Y. Hu, X.W. Lou, Assembling carbon-coated α -Fe₂O₃ hollow nanohorns on the CNT backbone for superior lithium storage capability, *Energy Environ. Sci.* 5 (2012) 5252–5256.
- N.S. Miriam Keppeler, Shubha Nageswaran, Madhavi Srinivasan, Synthesis of α -Fe₂O₃/carbon nanocomposites as high capacity electrodes for next generation lithium ion batteries: a review, *J. Mater. Chem. A* 4 (2016) 18223–18239.
- J.-G. Wang, Y. Yang, Z.-H. Huang, F. Kang, MnO-carbon hybrid nanofiber composites as superior anode materials for lithium-ion batteries, *Electrochim. Acta* 170 (2015) 164–170.
- B. Joshi, E. Samuel, H.S. Jo, Y.-I. Kim, S. Park, M.T. Swihart, W.Y. Yoon, S.S. Yoon, Carbon nanofibers loaded with carbon nanotubes and iron oxide as flexible freestanding lithium-ion battery anodes, *Electrochim. Acta* 253 (2017) 479–488.
- S. Qiu, X. Wang, G. Lu, J. Liu, C. He, Facile synthesis of MnO and nitrogen-doped carbon nanocomposites as anode material for lithium ion battery, *Mater. Lett.* 136 (2014) 289–291.
- M. Srivastava, J. Singh, T. Kuila, R.K. Layek, N.H. Kim, J.H. Lee, Recent advances in graphene and its metal-oxide hybrid nanostructures for lithium-ion batteries, *Nanoscale* 7 (2015) 4820–4868.
- H. Tabassum, R. Zou, A. Mahmood, Z. Liang, Q. Wang, H. Zhang, S. Gao, C. Qu, W. Guo, S. Guo, A universal strategy for hollow metal oxide nanoparticles encapsulated into B/N Co-doped graphitic nanotubes as high-performance lithium-ion battery anodes, *Adv. Mater.* 30 (2018).
- Xiao Han, Wen-Miao Chen, Xiguang Han, Y.-Z. Tanc, A.D. Sun, Nitrogen-rich MOF derived porous Co₃O₄/N-C composites with superior performance in lithium ion batteries, *J. Mater. Chem. A* 4 (2016) 13040–13045.
- Fan Wang, Hong-Yan Zhuo, Xiguang Han, W.-M. Chen, A.D. Sun, Foam-like CoO@N,S-codoped carbon composites derived from a well-designed N,S-rich Co-MOF for lithium ion batteries, *J. Mater. Chem. A* 5 (2017) 22964–22969.
- Zhongchao Bai, Yaohui Zhang, Yuwen Zhang, Chunli Guo, B. Tanga, A.D. Sun, MOFs-derived porous Mn₂O₃ as high-performance anode material for Li-ion battery, *J. Mater. Chem. A* 3 (2015) 5266–5269.
- G. de Combarieu, M. Morcrette, F. Millange, N. Guillou, J. Cabana, C.P. Grey, I. Margiolaki, G. Fe'rey, J.-M. Tarascon, Influence of the benzoquinone sorption on the structure and electrochemical performance of the MIL-53(Fe) hybrid porous material in a lithium-ion battery, *Chem. Mater.* 21 (2009) 1602–1611.
- A. Fateeva, P. Horcajada, T. Devic, C. Serre, J. Marrot, J.-M. Grenèche, M. Morcrette, J.-M. Tarascon, G. Maurin, G. Férey, Synthesis, structure, characterization, and redox properties of the porous MIL-68(Fe) solid, *Eur. J. Inorg. Chem.* 2010 (2010) 3789–3794.
- A. Banerjee, V. Aravindan, S. Bhatnagar, D. Mhamane, S. Madhavi, S. Ogale, Superior lithium storage properties of α -Fe₂O₃ nano-assembled spindles, *Nano Energy* 2 (2013) 890–896.
- X. Cao, B. Zheng, X. Rui, W. Shi, Q. Yan, H. Zhang, Metal oxide-coated three-dimensional graphene prepared by the use of metal-organic frameworks as precursors, *Angew. Chem.* 53 (2014) 1404–1409.
- R. Wu, X. Qian, X. Rui, H. Liu, B. Yadian, K. Zhou, J. Wei, Q. Yan, X.Q. Feng, Y. Long, L. Wang, Y. Huang, Zeolitic imidazolate framework 67-derived high symmetric porous Co₃O₄ hollow dodecahedra with highly enhanced lithium storage capability, *Small* 10 (2014) 1932–1938.
- Y. Zhang, Y.-B. Niu, T. Liu, Y.-T. Li, M.-Q. Wang, J. Hou, M. Xu, A nickel-based metal-organic framework: a novel optimized anode material for Li-ion batteries, *Mater. Lett.* 161 (2015) 712–715.
- Q. Li, G. Huang, D. Yin, Y. Wu, L. Wang, Synthesis of porous NiO nanorods as high-performance anode materials for lithium-ion batteries, *Part. Part. Syst. Char.* 33 (2016) 764–770.
- R. Wu, D.P. Wang, X. Rui, B. Liu, K. Zhou, A.W. Law, Q. Yan, J. Wei, Z. Chen, In-situ formation of hollow hybrids composed of cobalt sulfides embedded within porous

- carbon polyhedra/carbon nanotubes for high-performance lithium-ion batteries, *Adv. Mater.* 27 (2015) 3038–3044.
- [30] Z. Chen, R. Wu, M. Liu, H. Wang, H. Xu, Y. Guo, Y. Song, F. Fang, X. Yu, D. Sun, General synthesis of dual carbon-confined metal sulfides quantum dots toward high-performance anodes for sodium-ion batteries, *Adv. Funct. Mater.* 27 (2017) 1702046.
- [31] Hao Wang, Ziliang Chen, Yang Liu, Xu Hongbin, Licheng Cao, H. Qingc, A.R. Wu, Hierarchically porous-structured $Zn_xCo_{1-x}S@C-CNT$ nanocomposites with high-rate cycling performance for lithium-ion batteries, *J. Mater. Chem. A* 5 (2017) 23221–23227.
- [32] F. Wu, S. Zhang, B. Xi, Z. Feng, D. Sun, X. Ma, J. Zhang, J. Feng, S. Xiong, Unusual formation of $CoO@C$ “Dandelions” Derived from 2D kagóme MOFs for efficient lithium storage, *Adv. Energy Mater.* (2018) 1703242.
- [33] Y. Chu, L. Guo, B. Xi, Z. Feng, F. Wu, Y. Lin, J. Liu, D. Sun, J. Feng, Y. Qian, S. Xiong, Embedding $MnO@Mn_3O_4$ nanoparticles in an N-doped-carbon framework derived from mn-organic clusters for efficient lithium storage, *Adv. Mater.* 30 (2018).
- [34] O.M. Yaghi, H. Hayashi, R. Banerjee, K.S. Park, B. Wang, A. Cote, Preparation of functionalized zeolitic frameworks, in, *Google Patents*, 2017.
- [35] L.S. Xianglian Song, Xiaoying Chena, Tao Zhang, The characterization of graphene prepared using a nickel film catalyst pre-deposited to fused silica, *RSC Adv.* 6 (2016) 22244–22249.
- [36] Z. Ni, Y. Wang, T. Yu, Z. Shen, Raman spectroscopy and imaging of graphene, *Nano Res.* 1 (2010) 273–291.
- [37] Y. Jung, W. Yang, C.Y. Koo, K. Song, J. Moon, High performance and high stability low temperature aqueous solution-derived Li–Zr co-doped ZnO thin film transistors, *J. Mater. Chem.* 22 (2012) 5390.
- [38] <https://xpsimplified.com/elements/nickel.php#appnotes>, in.
- [39] B. Pal, D. Sarkar, P.K. Giri, Structural, optical, and magnetic properties of Ni doped ZnO nanoparticles: Correlation of magnetic moment with defect density, *Appl. Surf. Sci.* 356 (2015) 804–811.
- [40] M.-S. Wu, H.-W. Chang, Self-assembly of NiO-coated ZnO nanorod electrodes with core-shell nanostructures as anode materials for rechargeable lithium-ion batteries, *J. Phys. Chem. C* 117 (2013) 2590–2599.
- [41] Q. Wang, C.-Y. Zhang, W.-F. Shan, L.-L. Xing, X.-Y. Xue, Uniformly loading NiO nanowalls on graphene and their extremely high capacity and cyclability as anodes of lithium-ion batteries, *Mater. Lett.* 118 (2014) 66–68.
- [42] L. Xiao, D. Mei, M. Cao, D. Qu, B. Deng, Effects of structural patterns and degree of crystallinity on the performance of nanostructured ZnO as anode material for lithium-ion batteries, *J. Alloy. Compd.* 627 (2015) 455–462.
- [43] J. Li, D. Yan, S. Hou, T. Lu, Y. Yao, D.H.C. Chua, L. Pan, Metal-organic frameworks derived yolk-shell ZnO/NiO microspheres as high-performance anode materials for lithium-ion batteries, *Chem. Eng. J.* 335 (2018) 579–589.